

See discussions, stats, and author profiles for this publication at: <https://www.researchgate.net/publication/273468499>

Ball Milling Synthesized MnO_x as Highly Active Catalyst for Gaseous POPs Removal: Significance of Mechanochemically Induced Oxygen Vacancies

ARTICLE in ENVIRONMENTAL SCIENCE AND TECHNOLOGY · MARCH 2015

Impact Factor: 5.33 · DOI: 10.1021/es505232f · Source: PubMed

READS

78

10 AUTHORS, INCLUDING:



Jun Huang

Tsinghua University

133 PUBLICATIONS 3,049 CITATIONS

SEE PROFILE



Shubo Deng

Tsinghua University

153 PUBLICATIONS 3,822 CITATIONS

SEE PROFILE



Bin Wang

Tsinghua University

94 PUBLICATIONS 923 CITATIONS

SEE PROFILE



Yujue Wang

Tsinghua University

60 PUBLICATIONS 459 CITATIONS

SEE PROFILE

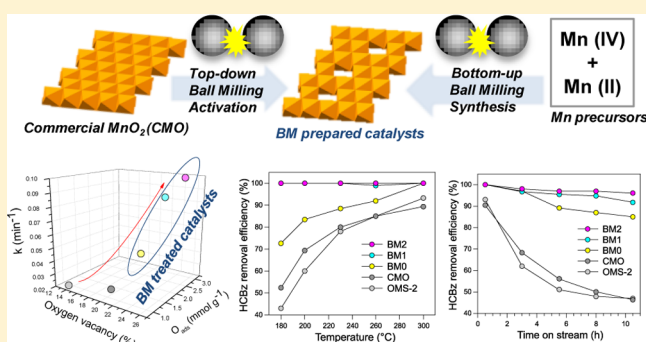
Ball Milling Synthesized MnO_x as Highly Active Catalyst for Gaseous POPs Removal: Significance of Mechanochemically Induced Oxygen Vacancies

Yang Yang, Shuzhen Zhang, Siwen Wang, Kunlun Zhang, Haizhu Wang, Jun Huang, Shubo Deng, Bin Wang, Yujue Wang, and Gang Yu*

School of Environment, Beijing Key Laboratory for Emerging Organic Contaminants Control, State Key Joint Laboratory of Environment Simulation and Pollution Control (SKLESPC), Tsinghua University, Beijing 100084, China

S Supporting Information

ABSTRACT: A rapid (1.5 h) one-step ball milling (BM) method was developed not only to modify commercial MnO_2 via top-down approaches (BM0), but also to bottom-up synthesize MnO_x by cogrinding of KMnO_4 and $\text{MnC}_4\text{H}_6\text{O}_4$ (BM1) or KMnO_4 and MnSO_4 (BM2). Catalysts activity on gaseous POPs removal was tested using hexachlorobenzene (HCBz) as surrogate. Catalytic performance decreases in the order of $\text{BM2} \approx \text{BM1}$ ($T_{90\%} = 180\text{--}200\text{ }^\circ\text{C}$) $>$ BM0 ($260\text{ }^\circ\text{C}$) $>$ $\text{CMO} \approx \text{cryptomelane MnO}_2$ ($>300\text{ }^\circ\text{C}$). Both adsorption and destruction contribute to HCBz removal at $180\text{ }^\circ\text{C}$ while destruction prevails at $200\text{--}300\text{ }^\circ\text{C}$. Mechanism studies show that destruction activity is lineally correlated with the amount of surface reactive oxygen species (O_{ads}); stability is determined by the removal of surface chloride, which is associated with the mobility of bulk lattice oxygen (O_{lat}); adsorption capacities are linearly correlated with surface area and pore structure. With the aid of extensive characterizations the excellent performance of BM prepared samples can be explained as (1) abundant surface vacancies enhance the generation of O_{ads} ; (2) massive bulk vacancies promote the mobility of bulk O_{lat} ; (3) large surface area and uniform pore size distribution facilitate the physisorption of HCBz.



INTRODUCTION

Waste incineration¹ and various thermal industrial processes² unintentionally produce gaseous POPs, including polychlorinated dibenzo-p-dioxins and dibenzofurans (PCDD/Fs), polychlorinated biphenyls (PCBs), hexachlorobenzene (HCBz) and pentachlorobenzene (PeCBz). In the past decades, destruction of gaseous POPs based on $\text{V}_2\text{O}_5\text{--WO}_3/\text{TiO}_2$ catalysts was extensively investigated.^{3,4} Our recent study found that manganese oxides (MnO_x) bulk catalysts showed higher activity than $\text{V}_2\text{O}_5\text{--WO}_3/\text{TiO}_2$.⁵ To further improve their activity as well as stability is of theoretical and practical significance and remains a steep challenge.

In view of the related researches that focus on CO and VOCs oxidation, a general conclusion can be found that increasing the abundance of surface oxygen vacancies can enhance catalyst oxidative activity.^{6–8} Several strategies have been reported to increase surface oxygen vacancies on MnO_x , including metal doping,⁹ ion exchange,¹⁰ and manipulations with morphology⁷ and crystallinity.¹¹ However, these methods are either complicated or time-consuming. One must notice that for the construction of pilot or full-scale catalytic treatment unit, a large amount of catalyst is required to cast honeycomb or catalytic filter modules. Obviously, most of the lab-scale

preparation methods cannot fulfill the industrial requirement. Thus, it is crucial to develop facile approaches for scale-up production of catalysts with abundant oxygen vacancies.

Recently, there has been an increasing interest in the mechanochemical synthesis of heterogeneous catalysts. Various metal oxides with abundant oxygen vacancies can be rapidly synthesized via ball milling (BM) procedure.^{12–14} Several studies have pointed out that perovskite^{15,16} and binary metal oxides¹⁷ prepared by BM methods outperform their counterparts synthesized by conventional solvent-based routes. To date, only few articles reported the synthesis of MnO_x with cryptomelane^{18,19} and pyrolusite²⁰ structure. Obviously more works are needed to broaden the environmental application of mechanochemically synthesized MnO_x for POPs removal and further investigate the role of mechanically induced oxygen vacancies in this specific reaction.

In this paper, BM methods was developed not only to synthesize MnO_x catalyst via bottom-up approaches but also to

Received: October 26, 2014

Revised: February 10, 2015

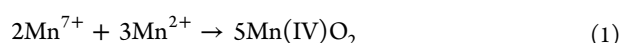
Accepted: March 11, 2015



modify commercial MnO₂ (CMO) via top-down approaches. Exceptional high performance of BM prepared samples was observed on HCBz removal. Combining with various characterization techniques, the important roles of oxygen vacancies on HCBz destruction activity and catalyst stability are revealed for the first time.

■ EXPERIMENTAL SECTION

Catalyst Preparation. CMO was obtained from Beijing Modern Estern Finechemical. BM0 was synthesized by the BM of CMO via top-down approach: 2.8 g CMO was charged into stainless steel (SS) milling pot (100 mL) with approximately 30 balls (5.5 mm size). The pot was sealed with ambient air and placed in a planetary ball mill (QM-3SP2, Nanjing University Instrument, China). The rotation speed of the planetary disk was set as 500 rpm and duration of 1.5 h. Bottom-up approaches were designed according to the redox reaction between Mn precursors:



BM1 refers to the samples generated from the 1.5 h milling of KMnO₄ (2 g) and MnC₄H₆O₄·4H₂O (4.6 g). BM2 refers to the samples generated from 1.5 h milling of KMnO₄ (2 g) and MnSO₄·H₂O (3.2 g). The resultant powders were washed out by deionized (DI) water, and dried at 110 °C for 4 h.

Cryptomelane-type MnO₂, well-known as octahedral molecular sieve (OMS-2), has attracted numerous attentions due to its high activity toward VOCs^{8,21} and POPs destruction.⁵ Therefore, it was chosen as a reference catalyst. OMS-2 was synthesized by 12 h hydrothermal method^{11,22} with details showing in Supporting Information (SI) Text S1.

Elemental analysis (SI Table S1) shows that OMS-2 has the highest amount of K⁺, which is contributed by K⁺ inside the tunnel structure.²³ Relatively small amount of K⁺ originated from KMnO₄ precursor was found on BM1 and BM2. To investigate the influence of K⁺, control sample BM0_K was prepared by cogrinding of 2.8 g CMO and 1.3 g KNO₃. The presence of Fe, coming from the jar and ball, was detected in all of the BM prepared samples (SI Table S1). To exclude Fe contaminant, BM0_{Zr} was synthesized by top-down approach with ball and jar made of zirconium oxide.

All the obtained powder catalysts were hydrolytically compressed, crushed, and sieved to catalyst pellets in sizes of 0.25–0.42 mm.

Catalyst Characterization. Catalysts were characterized by X-ray diffraction (XRD), X-ray photoelectron spectroscopy (XPS), field emission electron microscopy (FESEM), inductively coupled plasma atomic emission spectroscopy (ICP-AES), N₂ adsorption–desorption, H₂-temperature-programmed reduction (H₂-TPR), oxygen temperature-programmed desorption (O₂-TPD), and NH₃ temperature-programmed desorption (NH₃-TPD). The detail descriptions can be found in SI Text S2.

Flow-Stream Activity Test. A homemade heterogeneous catalytic reactor was adopted to test the activity of catalysts toward gaseous HCBz destruction. The configuration of reactor has been described previously.^{5,24} Briefly, HCBz (Accustandard, New Haven, CT) was placed inside the heating chamber and gradually vaporized at elevating temperature. The vapor was mixed with 300 mL min^{−1} carrier gas, forming the simulated flue gas with gaseous HCBz concentration of 5.5 ± 0.3 mg/Nm³. A fix-bed reactor was connected downstream to the gas

generator. Twenty mg of the catalyst pellets was placed in the quartz reactor supported by quartz wool, forming a catalyst bed with the space velocity (SV) of 450 000 mL g^{−1} catalyst h^{−1}. Off-gas was accumulatively sampled by impinge bottle filled with 1:1 acetone/hexane at 0 °C.

In short-term activity test, the reaction period was set as 30 min. Off-gas sampling was started from the beginning of the reaction. Fresh catalyst was used in each run and triplicates were performed at each temperature. As for the long-term adsorption or stability test, catalyst was continuously exposed to gaseous HCBz in N₂ or 10% O₂/N₂ for 10.5 h. The 30 min off-gas sampling was conducted at the interval of 2 h. Cumulative sampling lasted for the entire reaction was also performed to investigate the total amount of removed HCBz. After sampling, adsorptive solvent was spike with internal standard (1,2,4,5-tetrabromobenzene, Accustandard), and analyzed by GC-ECD (Agilent 6890N). Residual HCBz on catalysts was ultrasonically extracted (twice by 15 mL hexane) at room temperature and analyzed by GC as well.

The removal efficiency (RE), adsorption efficiency (AE), and destruction efficiency (DE) are defined as follows:

$$\text{RE}(\%) = \frac{(R_{\text{in}} - R_{\text{out}})}{R_{\text{in}}} \times 100\% \quad (2)$$

$$\text{AE}(\%) = \frac{R_{\text{cat}}}{R_{\text{in}}} \times 100\% \quad (3)$$

$$\text{DE}(\%) = \text{RE}(\%) - \text{AE}(\%) \quad (4)$$

where R_{in} (μg) and R_{out} (μg) are the amount of inlet and outlet HCBz, respectively. R_{cat} (μg) is the amount of HCBz extracted from catalyst.

In some cases, surface chloride (Cl[−]) was ultrasonically extracted from spent catalysts by DI water and quantified by ionic chromatography (Dionex ICS-2000). The selectivity of surface Cl[−] was calculated as follows:

$$\text{surfaceCl}^{-}\text{selectivity}(\%) = \frac{N}{M \times 6} \times 100\% \quad (5)$$

where M (mol) is the total amount of destructed HCBz. N (mol) is the Cl[−] extracted from spent catalyst.

Batch Activity Test. The procedure of batch reaction can be referred to previous studies.^{5,24} HCBz was spiked on catalyst powder to reach a loading of 40 mg (HCBz) g^{−1} catalyst. The resulting mixture was charged into 25 mL glass ampules, sealed with air, and then placed in the furnace at 300 °C. Once the predetermine reaction periods (10, 20, and 30 min) were reached, ampules were moved out from the furnace and quenched to room temperature, and then crushed and ultrasonically extracted by hexane. The residual HCBz and intermediates in extract were analyzed by GC-MS (Shimadzu QP2010). Triplicates test were performed at each reaction period.

■ RESULTS AND DISCUSSION

Catalyst Characterization. The FESEM images (SI Figure S1) show that BM prepared catalysts are in the form of irregular particles with rough surface. SI Figure S2 shows the XRD and Raman patterns of catalysts. The reference catalysts OMS-2 and CMO are well crystallized, while BM0, BM1, and BM2 present amorphous structure. Raman characterization

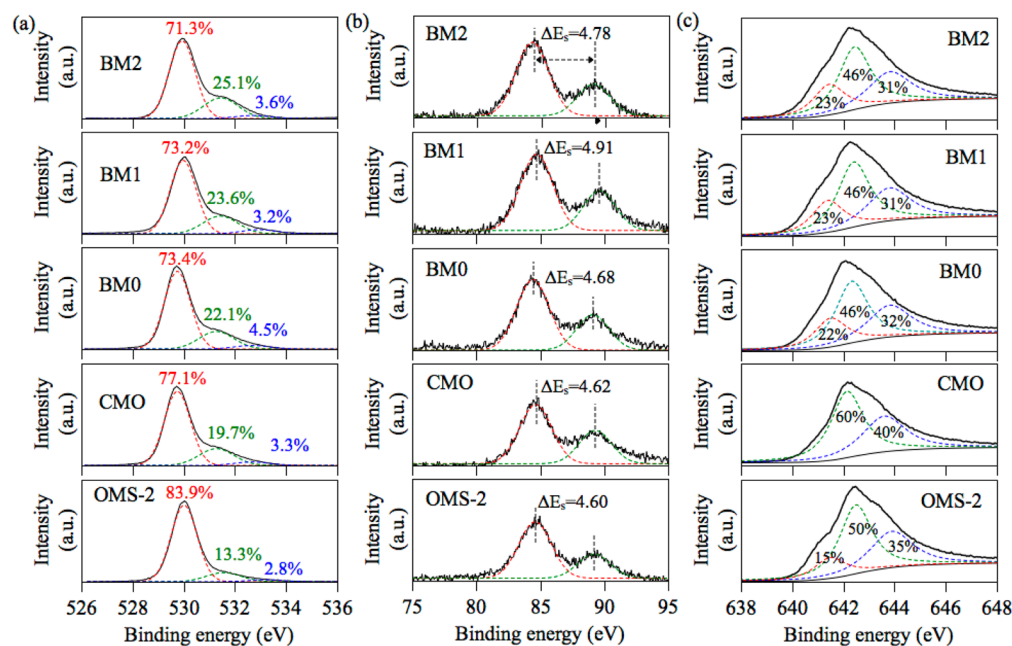


Figure 1. O 1s (a) and Mn 3s (b) XPS spectra of catalysts.

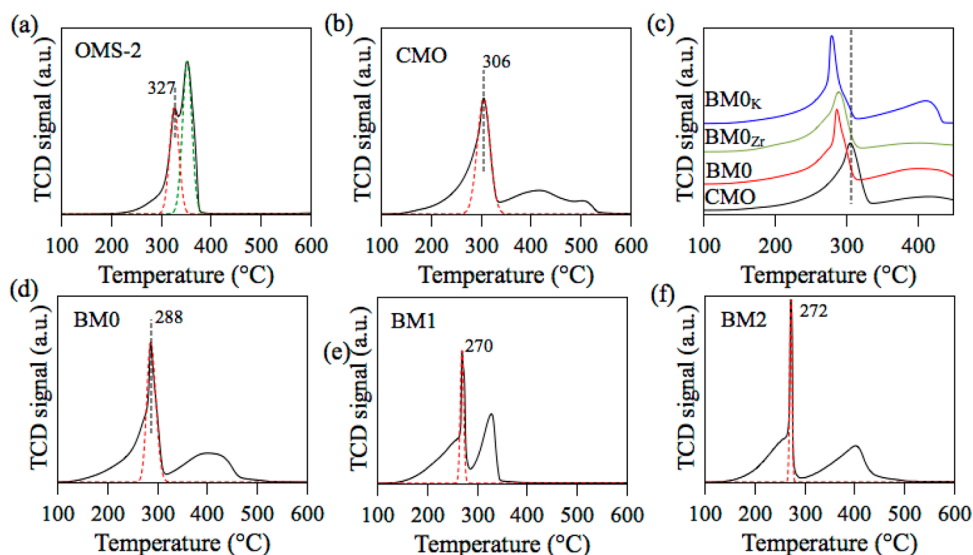


Figure 2. H_2 -TPR profiles of catalysts.

shows that the Mn–O lattice bonds of BM prepared amorphous samples are highly distorted.

The specific surface area of BM0 ($84 \text{ cm}^2 \text{ g}^{-1}$) is twice as that of CMO (SI Table S1). The improvement of textural properties is expected as the particle size reduction induced by mechanical force. BM1 ($267 \text{ cm}^2 \text{ g}^{-1}$) and BM2 ($200 \text{ cm}^2 \text{ g}^{-1}$) have even larger specific surface area, which is comparable with that of MnO_x synthesized by multistep procedures such as coprecipitation ($275\text{--}330 \text{ m}^2 \text{ g}^{-1}$),^{8,25} and template method ($213 \text{ m}^2 \text{ g}^{-1}$).²⁶ Pore size distribution analyses (SI Figure S3) show that CMO, BM0, BM1, and BM2 have uniform pores around 3.3–6 nm.

The surface state of element O and Mn were investigated by XPS. Three types of surface oxygen species can be identified according to the O 1s spectra (Figure 1a):^{7,27,28} peak located at 529.8–530.3 eV is ascribed to lattice oxygen O^{2-} (O_{lat}); peak at 531.1–531.6 eV is assigned to the surface adsorbed species

(O_{ads}); peak at 533 eV is due to the adsorbed molecular water. The fraction of O_{ads} decreases in the order of $\text{BM2} > \text{BM1} > \text{BM0} > \text{CMO} > \text{OMS-2}$. The above tendency also represents the abundance of surface oxygen vacancies. Considering the O_{ads} is originated from the dissociative adsorption of O_2 molecule onto oxygen vacancies.^{29–32}

As shown in Figure 1b, the Mn 3s spectra show two separate peaks. The average oxidation state (AOS) of surface Mn was estimated based on the magnitude of Mn 3s doublet splitting (ΔE_s):^{10,33}

$$\text{AOS} = 8.956 - 1.126\Delta E_s \quad (6)$$

The AOS decreases in the order of $\text{OMS-2} (3.78) > \text{CMO} (3.75) > \text{BM0} (3.69) > \text{BM1} (3.43) > \text{BM2} (3.57)$. The lower AOS implies the higher fraction of Mn (II) and Mn (III), which is associated with the formation of oxygen vacancies (denoted as " \square " in eq 7 and 8):

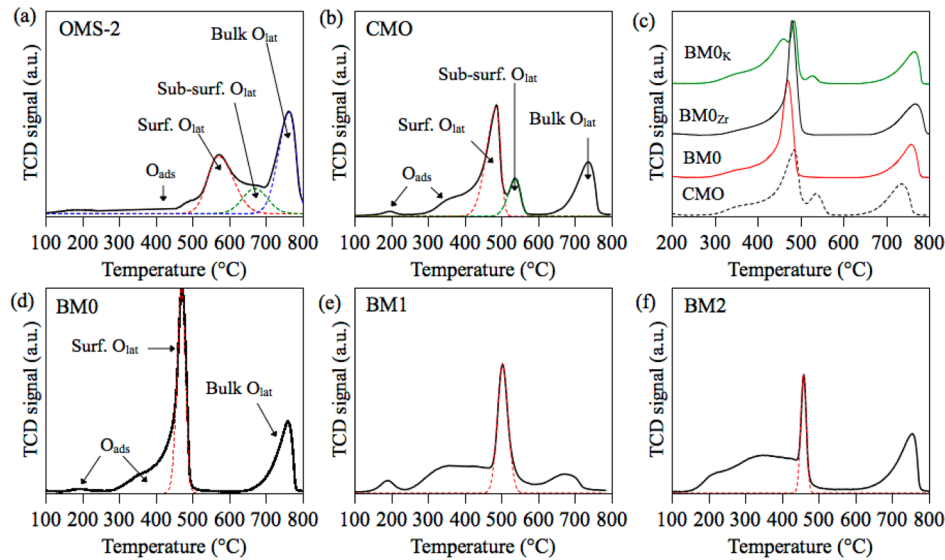


Figure 3. O₂-TPD profiles of catalysts.

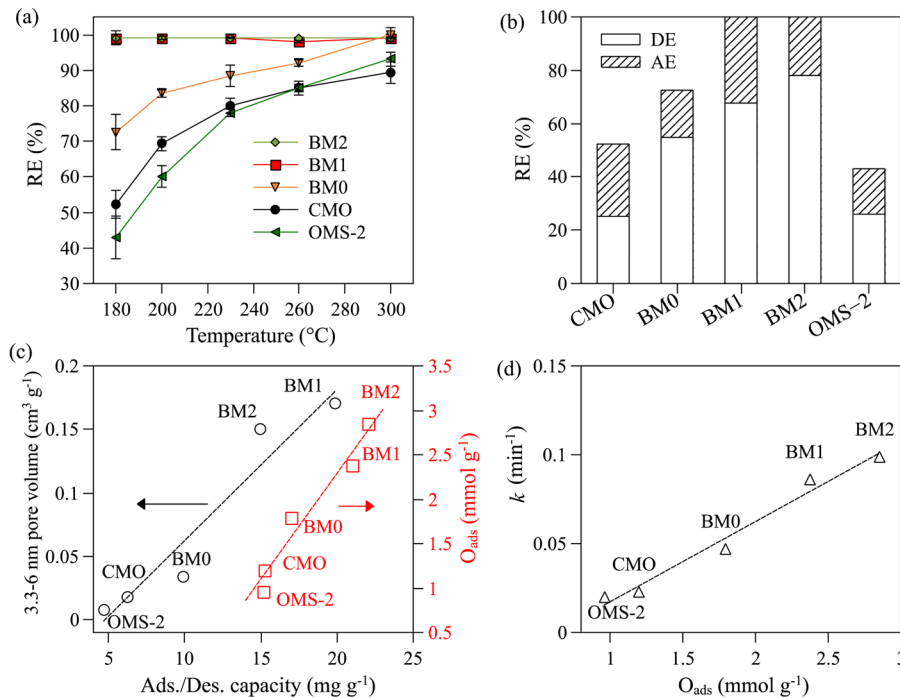
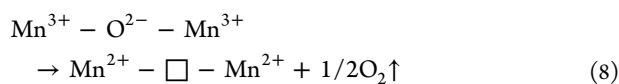
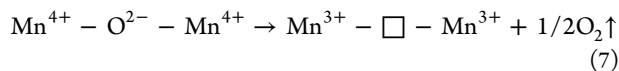


Figure 4. (a) Short-term activity as a function of temperature. (b) Contribution of DE and AE at 180 °C. (c) Equilibrium adsorption and destruction capacity obtained at 180 °C in N₂ flow. (d) Correlation between O_{ads} quantity and kinetic constant.



The deconvolution of Mn 2p_{3/2} peak (Figure 1c) provides additional evidence. Three peaks with binding energy of 641, 642, and 643 eV are associated with Mn²⁺, Mn³⁺, and Mn⁴⁺, respectively.^{6,27} Obviously, the BM prepared MnO_x have higher fraction of Mn²⁺ and Mn³⁺ than CMO and OMS-2.

Theoretically, in BM process the friction and collision of ball could create high temperature (>1000 °C) at local area (ca. 1 μm²) for short periods (10⁻³–10⁻⁴ s).^{12,34} Such high energy

input is sufficient to cause the dislodging of surface O_{lat}, which explains the increase of oxygen vacancies from CMO to BM0 after top-down modification. In the case of BM1 and BM2 prepared by bottom-up approaches, Mn precursors are intimately mixed to initiate redox reaction 1, but the growth of MnO_x particles is inhibited due to the intensive fraction and impact on interfaces. Therefore, in addition to the abundant surface vacancies, BM1 and BM2 have large specific surface area.

The influence of oxygen vacancies on redox properties was characterized by H₂-TPR. As illustrated in Figure 2, the first reduction peak at low temperature indicates the reduction from MnO₂ to Mn₃O₄, while the second peak indicates the change from Mn₃O₄ to MnO.^{27,35} Judging from the position of first

reduction peak, the redox properties decreases in the order of $\text{BM2} \approx \text{BM1} > \text{BM0} > \text{CMO} > \text{OMS-2}$. The enhanced reactivity observed on the BM prepared samples can be ascribed to the increase of oxygen vacancies, which promote the reactivity and mobility of surface lattice oxygen. The TPR patterns of BM0_{Zr} and BM0_{K} are similar to that of BM0 (Figure 2c), implying that the Fe and K doping has negligible effect on redox properties.

Aside from the distinguished reduction peaks, shoulder peaks appear before the first reduction peaks. These peaks represent the H_2 consumption by surface O_{ads} , which are not strongly stabilized within the lattice.²⁷ The amount of H_2 consumption (SI Table S2), which could be considered as an indirect titration of O_{ads} , decreases as $\text{BM2} \approx \text{BM1} > \text{BM0} > \text{AMO} > \text{OMS-2}$. Assuming MnO is the final reduction product, the bulk Mn valence of catalysts can be estimated based on total H_2 consumption (SI Table S2): CMO (3.54) > OMS-2 (3.40) > BM0 (3.30) > BM2 (3.00) \approx BM1 (2.95).

In order to quantify surface oxygen species and investigate the mobility of O_{lat} , O_2 -TPD analyses were performed (Figure 3). The oxygen desorption peaks can be classified as follows:^{27,36} desorption of adsorbed peroxy species $\text{O}_2^-_{\text{ads}}$ (100–300 °C), desorption of adsorbed monatomic species O^-_{ads} (300–400 °C), release of surface O_{lat} (400–600 °C), and evolution of bulk O_{lat} (>600 °C). The deconvolution analyses of Figure 3a and b indicate the presence of additional peak between the surface O_{lat} and bulk O_{lat} desorption peaks, which might be assigned to the desorption of subsurface O_{lat} .³⁷

The amount of O_{ads} was quantified by integrating the area under TPD curves. As summarized in SI Table S2, BM2 and BM1 have the most abundant O_{ads} , followed by BM0, CMO, and OMS-2. This trend roughly meets the indirect titration by H_2 -TPR and it is also in good accordance with the abundance of oxygen vacancies obtained from XPS analyses.

In addition to surface vacancies, bulk vacancies are also created by BM approaches. As can be found in SI Table S2, BM0 have lower total H_2 consumption and O_2 desorption quantity than CMO, which can be interpreted as the loss of bulk O_{lat} after top-down BM. Bottom-up BM approaches might lead to the same results. Because the measured average Mn valence of BM1 and BM2 is significantly lower than the tetravalence predicted by reaction 1. The loss of bulk O_{lat} creates bulk oxygen vacancies, which become the migration pathways of bulk O_{lat} .^{38,39} For instance, the desorption peak of subsurface O_{lat} is distinctive in the O_2 -TPD spectra of CMO but this peak vanishes on BM0 (Figure 3b vs 3d). Similar results are observed on BM0_{Zr} and BM0_{K} as well (Figure 3c). These data clearly suggest that the diffusion of O_{lat} from bulk to surface is facilitated after BM treatment.

Catalyst Activity. Figure 4a shows the HCBz removal performance of MnO_x catalysts as a function of temperature. By comparing the $T_{90\%}$ reaction temperature (at which 90% DE is achieved), the general decreasing catalytic performance is $\text{BM2} \approx \text{BM1}$ (between 180 and 200 °C) > BM0 (260 °C) > $\text{CMO} \approx \text{OMS-2}$ (>300 °C). The best-performing BM2 exhibits the highest specific activity among the reported data (SI Table S3). The performances of BM0_{K} and BM0_{Zr} are superior to that of CMO but similar to that of BM0 (SI Figure S4). These results rule out the possibility of Fe and K doping as the reason for promoted activity. Unfortunately neither carbon or chlorine balance could be established in the flow-stream test due to the low inlet concentration of HCBz. Nevertheless, organic intermediates could only be found in the fore coming batch

reaction but not in the adsorptive solvents of flow stream tested by GC-MS operated in both SCAN and SIM modes.

It is also important to notice that all the samples exhibit adsorbent-catalyst dual function at 180 °C as the RE is contributed by both destruction and adsorption (Figure 4b). To measure the adsorption capacity, catalysts were exposed to gaseous HCBz in N_2 flow at 180 °C for 10–10.5 h to achieve adsorption equilibrium. NH_3 -TPD analyses (SI Figure S5) taking BM2 as an example show that although more surface vacancies are created in N_2 atmosphere, the properties of vacancies are rarely changed after HCBz adsorption. This finding excludes the possibility that the adsorption is conducted by the chemical interaction between HCBz and vacancies. It is found that the HCBz adsorption capacity decreases as BM1 (20.0) > BM2 (15.0) > BM0 (9.9) > CMO (6.2) > OMS-2 (4.7 mg g^{-1}). This tendency is coherent with the BET surface area but aberrance was found on OMS-2 and CMO. Better correlation was found between adsorption capacity and pore volume between 3.3 and 6 nm (Figure 4c), which is the dominant pore size of CMO, BM0, BM1, and BM2. Considering this pore size dependent adsorption character and the high boiling point of HCBz, it could be inferred that the adsorption mechanism is associated with the capillary condensation.

Aside from adsorption, destruction of HCBz was found in the absence of gaseous O_2 . Destruction capacities are calculated as follows: BM2 (22.1) > BM1 (21.0) > BM0 (17.0) > CMO (15.2) > OMS-2 (15.1 mg g^{-1}). Although gaseous destruction products cannot be detected, residual Cl^- is found on spent catalysts (3.0 μmol for BM2, 2.0 μmol for BM1, and 0.4 μmol for BM0). The destruction of HCBz in the absence of gaseous O_2 can be explained by Mars-van-Krevelen mechanism: instead of reacting with gaseous O_2 , HCBz is oxidized by surface reactive oxygen species, creating oxygen vacancies. The consumed reactive oxygen species are subsequently regenerated via the dissociative adsorption of gaseous O_2 on vacancies. Even though this theory has recently gained wide application for explaining CO and VOC oxidation over MnO_x , controversial conclusions were reported regarding the active species being O_{ads} ⁷ or surface O_{lat} .^{11,21}

In this study, O_{ads} was identified as the active sites for HCBz destruction based on following experimental supports: (1) The direct evidence comes from the linear correlation between the destruction capacities and the amount of O_{ads} (Figure 4c). (2) H_2 -TPR proves that O_{ads} has sufficient high oxidative activity at 180 °C. (3) the amount of O_{ads} fulfill the quantitative demand for HCBz destruction. According to the stoichiometry $\text{C}_6\text{Cl}_6 + 6\text{O}_2 \rightarrow 6\text{CO}_2 + 3\text{Cl}_2$, the complete destruction of HCBz requires 0.32 to 0.47 mmol O_{ads} per gram of catalyst, which is still lower than the amount of O_{ads} measured by O_2 -TPD.

Batch reaction was designed to investigate the intrinsic of destruction reaction. As can be found in SI Figure S6, the reaction follows pseudo-first order kinetics. The observed rate constant k decreases in the order of BM2 (0.099) > BM1 (0.086) > BM0 (0.047) > CMO (0.023) > OMS-2 (0.019 min^{-1}). Linear correlation was also found between k and the amount of O_{ads} (Figure 4d). This provides additional evidence that O_{ads} is the active sites for HCBz destruction.

Pentachlorobenzene (PeCBz) and hexachlorobutadiene (C_4Cl_6) were detected as intermediates (SI Figure S7) over all the catalysts. The former represents the cleavage of cleavage of C–Cl bond and protonation of HCBz on surface hydroxyl group, while the latter indicates the benzene-ring rupture

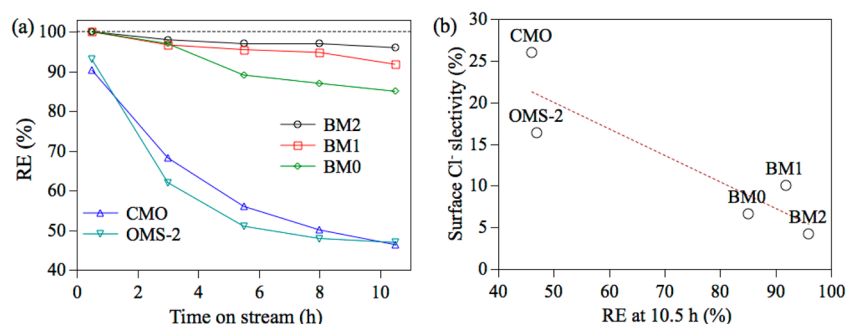


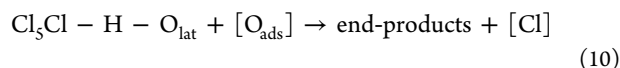
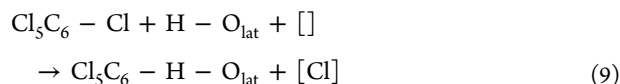
Figure 5. (a) Stability test of catalysts and (b) selectivity of surface Cl.

caused by the nucleophilic attack of reactive oxygen species.^{5,40} These results also imply that reaction mechanism was not altered by the increase of vacancies. Hence the promotion of catalytic activity brought by BM treatment could be assigned to the increasing number of active sites.

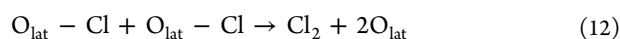
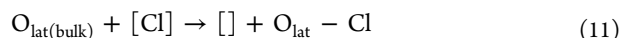
Stability and TOF Calculation. Stability of catalysts was investigated by continuously operating the HCBz destruction reaction at 300 °C for 10.5 h. As shown in Figure 5a, BM prepared samples have better durability than OMS-2 and CMO.

Generally, surface chlorination is responsible for catalyst deactivation in the course of chlorinated organics destruction.^{41,42} The degree of surface chlorination was evaluated by calculating the surface Cl⁻ selectivity. A negative correlation between 10.5 h RE and surface Cl⁻ selectivity (Figure 5b) suggests that the resistance to chlorine poisoning determines the stability of catalyst.

The deposition and removal of surface Cl⁻ on MnO_x catalyst might share similar mechanism with Deacon reaction (4HCl + O₂ → 2H₂O + 2Cl₂).⁴³ The first elemental step is the dissociative adsorption of HCl on metal oxides, leaving Cl atom into the oxygen vacancies and transferring H atom to the top of surface O_{lat}.⁴⁴ Previously we found that surface Cl⁻ suppress the regeneration of O_{ads} on MnO_x.⁵ With the aid of NH₃-TPD analyses (SI Figure S5), the change of vacancy properties after HCBz destruction is validated. Therefore, it is suspected that the Cl atoms generated from the dissociative adsorption (reaction 9) and destruction (reaction 10) of HCBz may also occupy the oxygen vacancies ([]).



Computational simulation on CeO₂ shows that oxygen atoms from the bulk can diffuse toward the surface, pushing a [Cl] atom toward the outer surface, converting [Cl] into O_{lat}-Cl (reaction 11). Surface Cl⁻ was subsequently removed in the form of Cl₂ via the recombination of two O_{lat}-Cl (reaction 12).⁴⁵



This mechanism is also applicable to MnO₂ as Amrute et al.⁴⁶ recently proved that the bulk O_{lat} of MnO₂ involve in the Cl₂ production. The mobility of bulk O_{lat} might be the key of surface Cl⁻ removal. To verify this hypothesis, long-term tests

of BM2 were conducted in high space velocity (HSV) scenario (SV of 900 000 mL g⁻¹ h⁻¹ at 300 °C) and low temperature (LT) scenarios (SV of 450 000 mL g⁻¹ h⁻¹ at 230 or 180 °C). In HSV scenario, the surface residence time of HCBz was shortened, resulting in the decrease of 10.5 h RE from 96% to 76%. However, due to the high mobility of bulk O_{lat} at 300 °C, the surface Cl⁻ selectivity only slightly increase from 4.2 to 5.5%. In the case of LT scenario, bulk O_{lat} has lower mobility. As a result, significant Cl⁻ deposition (selectivity reaches 30% at 230 °C and 38% at 180 °C) and deactivation (10.5 h RE of 48% at 230 °C and 29% at 180 °C) are observed. Based on the above analyses, the high chlorine resistance of BM0, BM1, and BM2 can be explained as their high bulk O_{lat} mobility contributed by massive bulk vacancies.

As can be observed from Figure 5a, The RE of HCBz reached a plateau at 10.5 h, indicative of the equilibrium between consumption and regeneration at each active site. Thus, turnover frequency (TOF) can be calculated by eq 13, considering the O_{ads} as active sites and utilizing the first-order dependence on HCBz,

$$\text{TOF} = -\left(\frac{Q}{\eta}\right) \times C_{\text{HCBz}} \times \ln(1 - x) \quad (13)$$

where Q is the volumetric flow (Nm³ s⁻¹), C_{HCBz} is the inlet concentration of HCBz (μmol Nm⁻³), x is the RE at 10.5 h, η is the amount of O_{ads} (μmol) on 20 mg catalysts.

As shown in SI Table S2, BM0, BM1, and BM2 have higher TOF than OMS-2 and CMO. The results show that the excellent catalytic performance of BM prepared samples is not only due to the larger number of active sites, but also due to the higher conversion efficiency at each active site.

Since HCBz is a perfect surrogate of PCDD/Fs, PCBs, and PeCBz in catalytic destruction reaction,^{5,47} BM synthesized MnO_x with excellent HCBz removal performance is potentially effective for the destruction of other POPs. More over, the facile scalable catalyst production facilitates the construction of catalyst module. On the basis of this study, pilot-scale treatment of POPs in incineration flue gas is currently underway.

■ ASSOCIATED CONTENT

Supporting Information

Narratives, graphics and table addressing experimental details, catalyst characterization and comparison of activity. This material is available free of charge via the Internet at <http://pubs.acs.org>.

AUTHOR INFORMATION

Corresponding Author

*Phone: +86-10-62787137; fax: +86-10-62785687; e-mail: ygden@mail.tsinghua.edu.cn.

Notes

The authors declare no competing financial interest.

ACKNOWLEDGMENTS

This work was supported by National High Technology Research and Development Program of China (2013AA06A305), Program for Changjiang Scholars and Innovative Research Team in University (IRT1261), the Collaborative Innovation Center for Regional Environmental Quality.

REFERENCES

- (1) Wikstrom, E.; Tysklind, M.; Marklund, S. Influence of variation in combustion conditions on the primary formation of chlorinated organic micropollutants during municipal solid waste combustion. *Environ. Sci. Technol.* **1999**, *33* (23), 4263–4269.
- (2) Liu, G.; Zheng, M.; Liu, W.; Wang, C.; Zhang, B.; Gao, L.; Su, G.; Xiao, K.; Lv, P. Atmospheric emission of PCDD/Fs, PCBs, hexachlorobenzene, and pentachlorobenzene from the coking industry. *Environ. Sci. Technol.* **2009**, *43* (24), 9196–9201.
- (3) Weber, R.; Sakurai, T.; Hagenmaier, H. Low temperature decomposition of PCDD/PCDF, chlorobenzenes and PAHs by TiO₂-based V₂O₅-WO₃ catalysts. *Appl. Catal., B* **1999**, *20* (4), 249–256.
- (4) Hung, P. C.; Chang, S. H.; Lin, S. H.; Buekens, A.; Chang, M. B. Pilot tests on the catalytic filtration of dioxins. *Environ. Sci. Technol.* **2014**, *48* (7), 3995–4001.
- (5) Yang, Y.; Huang, J.; Wang, S.; Deng, S.; Wang, B.; Yu, G. Catalytic removal of gaseous unintentional POPs on manganese oxide octahedral molecular sieves. *Appl. Catal., B* **2013**, *142–143*, 568–578.
- (6) Hou, J.; Li, Y.; Liu, L.; Ren, L.; Zhao, X. Effect of giant oxygen vacancy defects on the catalytic oxidation of OMS-2 nanorods. *J. Mater. Chem. A* **2013**, *1* (23), 6736–6741.
- (7) Wang, F.; Dai, H.; Deng, J.; Bai, G.; Ji, K.; Liu, Y. Manganese oxides with rod-, wire-, tube-, and flower-like morphologies: Highly effective catalysts for the removal of toluene. *Environ. Sci. Technol.* **2012**, *46* (7), 4034–4041.
- (8) Genuino, H. C.; Dharmarathna, S.; Njagi, E. C.; Mei, M. C.; Suib, S. L. Gas-phase total oxidation of benzene, toluene, ethylbenzene, and xylenes using shape-selective manganese oxide and copper manganese oxide catalysts. *J. Phys. Chem. C* **2012**, *116* (22), 12066–12078.
- (9) Sun, L. A.; Cao, Q. Q.; Hu, B. Q.; Li, J. H.; Hao, J. M.; Jing, G. H.; Tang, X. F. Synthesis, characterization and catalytic activities of vanadium-cryptomelane manganese oxides in low-temperature NO reduction with NH₃. *Appl. Catal., A* **2011**, *393* (1–2), 323–330.
- (10) Santos, V. P.; Soares, O. S. G. P.; Bakker, J. J. W.; Pereira, M. F. R.; Órfão, J. J. M.; Gascon, J.; Kapteijn, F.; Figueiredo, J. L. Structural and chemical disorder of cryptomelane promoted by alkali doping: Influence on catalytic properties. *J. Catal.* **2012**, *293*, 165–174.
- (11) Liang, S. H.; Bulgan, F. T. G.; Zong, R. L.; Zhu, Y. F. Effect of phase structure of MnO₂ nanorod catalyst on the activity for CO oxidation. *J. Phys. Chem. C* **2008**, *112* (14), 5307–5315.
- (12) Ralphs, K.; Hardacre, C.; James, S. L. Application of heterogeneous catalysts prepared by mechanochemical synthesis. *Chem. Soc. Rev.* **2013**, *42* (18), 7701–7718.
- (13) Sepelak, V.; Begin-Colin, S.; Le Caer, G. Transformations in oxides induced by high-energy ball-milling. *Dalton Trans.* **2012**, *41* (39), 11927–11948.
- (14) Sepelak, V.; Duvel, A.; Wilkening, M.; Becker, K.-D.; Heitjans, P. Mechanochemical reactions and syntheses of oxides. *Chem. Soc. Rev.* **2013**, *42* (18), 7507–7520.
- (15) Petrović, S.; Terlecki-Baričević, A.; Karanović, L.; Kirilov-Stefanov, P.; Zdujic, M.; Dondur, V.; Paneva, D.; Mitov, I.; Rakić, V. LaMO₃ (M = Mg, Ti, Fe) perovskite type oxides: Preparation, characterization and catalytic properties in methane deep oxidation. *Appl. Catal., B* **2008**, *79* (2), 186–198.
- (16) Szabo, V.; Bassir, M.; Van Neste, A.; Kaliaguine, S. Perovskite-type oxides synthesized by reactive grinding: Part II: Catalytic properties of LaCo_(1-x)Fe_xO₃ in VOC oxidation. *Appl. Catal., B* **2002**, *37* (2), 175–180.
- (17) Kamolpoph, U.; Taylor, S. F. R.; Breen, J. P.; Burch, R.; Delgado, J. J.; Chansai, S.; Hardacre, C.; Hengrasmee, S.; James, S. L. Low-temperature selective catalytic reduction (SCR) of NO_x with n-octane using solvent-free mechanochemically prepared Ag/Al₂O₃ catalysts. *ACS Catal.* **2011**, *1* (10), 1257–1262.
- (18) Ding, Y.-s.; Shen, X.-f.; Sithambaram, S.; Gomez, S.; Kumar, R.; Crisostomo, V. M. B.; Suib, S. L.; Aindow, M. Synthesis and catalytic activity of cryptomelane-type manganese dioxide nanomaterials produced by a novel solvent-free method. *Chem. Mater.* **2005**, *17* (21), 5382–5389.
- (19) Meng, Y.; Song, W.; Huang, H.; Ren, Z.; Chen, S.-Y.; Suib, S. L. Structure–property relationship of bifunctional MnO₂ nanostructures: Highly efficient, ultra-stable electrochemical water oxidation and oxygen reduction reaction catalysts identified in alkaline media. *J. Am. Chem. Soc.* **2014**, *136* (32), 11452–11464.
- (20) Poinson, C.; Klein, H.; Strobel, P.; Roux, C.; Surcin, C. Electrochemical response of nanocrystalline tetragonal manganese dioxides prepared by spray vapor pyrolysis and ball milling. *J. Phys. Chem. C* **2007**, *111* (27), 9644–9651.
- (21) Luo, J.; Zhang, Q.; Garcia-Martinez, J.; Suib, S. L. Adsorptive and acidic properties, reversible lattice oxygen evolution, and catalytic mechanism of cryptomelane-type manganese oxides as oxidation catalysts. *J. Am. Chem. Soc.* **2008**, *130* (10), 3198–3207.
- (22) Wang, X.; Li, Y. Synthesis and formation mechanism of manganese dioxide nanowires/nanorods. *Chem.—Eur. J.* **2003**, *9* (1), 300–306.
- (23) Suib, S. L. Porous manganese oxide octahedral molecular sieves and octahedral layered materials. *Acc. Chem. Res.* **2008**, *41* (4), 479–487.
- (24) Yang, Y.; Yu, G.; Deng, S.; Wang, S.; Xu, Z.; Huang, J.; Wang, B. Catalytic oxidation of hexachlorobenzene in simulated gas on V₂O₅-WO₃/TiO₂ catalyst. *Chem. Eng. J.* **2012**, *192*, 284–291.
- (25) Ching, S.; Kriz, D. A.; Luthy, K. M.; Njagi, E. C.; Suib, S. L. Self-assembly of manganese oxide nanoparticles and hollow spheres. Catalytic activity in carbon monoxide oxidation. *Chem. Commun.* **2011**, *47* (29), 8286–8288.
- (26) Bastos, S. S. T.; Orfao, J. J. M.; Freitas, M. M. A.; Pereira, M. F. R.; Figueiredo, J. L. Manganese oxide catalysts synthesized by exotemplating for the total oxidation of ethanol. *Appl. Catal., B* **2009**, *93* (1–2), 30–37.
- (27) Santos, V. P.; Pereira, M. F. R.; Orfao, J. J. M.; Figueiredo, J. L. The role of lattice oxygen on the activity of manganese oxides towards the oxidation of volatile organic compounds. *Appl. Catal., B* **2010**, *99* (1–2), 353–363.
- (28) Tian, Z.-Y.; Tchoua Ngamou, P. H.; Vannier, V.; Kohse-Höinghaus, K.; Bahlawane, N. Catalytic oxidation of VOCs over mixed Co-Mn oxides. *Appl. Catal., B* **2012**, *117–118*, 125–134.
- (29) Bielanski, A.; Haber, J. *Oxygen in Catalysis*; Dekker: New York, 1991.
- (30) Gellings, P. J.; Bouwmeester, H. J. M. Solid state aspects of oxidation catalysis. *Catal. Today* **2000**, *58* (1), 1–53.
- (31) Pushkarev, V. V.; Kovalchuk, V. I.; d'Itri, J. L. Probing defect sites on the CeO₂ surface with dioxygen. *J. Phys. Chem. B* **2004**, *108* (17), 5341–5348.
- (32) Haber, J.; Turek, W. Kinetic studies as a method to differentiate between oxygen species involved in the oxidation of propene. *J. Catal.* **2000**, *190* (2), 320–326.
- (33) Santos, V. P.; Pereira, M. F. R.; Orfao, J. J. M.; Figueiredo, J. L. Synthesis and characterization of manganese oxide catalysts for the total oxidation of ethyl acetate. *Top. Catal.* **2009**, *52* (5), 470–481.
- (34) Balaz, P.; Achimovicova, M.; Balaz, M.; Billik, P.; Cherkezova-Zheleva, Z.; Criado, J. M.; Delogu, F.; Dutkova, E.; Gaffet, E.; Gotor, F. J.; Kumar, R.; Mitov, I.; Rojac, T.; Senna, M.; Streletsii, A.;

Wieczorek-Ciurowa, K. Hallmarks of mechanochemistry: From nanoparticles to technology. *Chem. Soc. Rev.* **2013**, 42 (18), 7571–7637.

(35) Park, T. S.; Jeong, S. K.; Hong, S. H.; Hong, S. C. Selective catalytic reduction of nitrogen oxides with NH_3 over natural manganese ore at low temperature. *Ind. Eng. Chem. Res.* **2001**, 40 (21), 4491–4495.

(36) Meng-Fei, L.; Ping, F.; Mai, H.; Yun-Long, X. In situ XRD, Raman, and TPR studies of $\text{CuO}/\text{Al}_2\text{O}_3$ catalysts for CO oxidation. *J. Mol. Catal., A: Chem.* **2005**, 239 (1–2), 243–248.

(37) Yu, L.; Diao, G.; Ye, F.; Sun, M.; Zhou, J.; Li, Y.; Liu, Y. Promoting effect of Ce in Ce/OMS-2 catalyst for catalytic combustion of dimethyl ether. *Catal. Lett.* **2011**, 141 (1), 111–119.

(38) Huang, T.-J.; Wang, C.-H. Roles of surface and bulk lattice oxygen in forming CO_2 and CO during methane reaction over gadolinia-doped ceria. *Catal. Lett.* **2007**, 118 (1), 103–108.

(39) Menon, U.; Galvita, V. V.; Marin, G. B. Reaction network for the total oxidation of toluene over $\text{CuO}-\text{CeO}_2/\text{Al}_2\text{O}_3$. *J. Catal.* **2011**, 283 (1), 1–9.

(40) Yang, Y.; Huang, J.; Zhang, S.; Wang, S.; Deng, S.; Wang, B.; Yu, G. Catalytic removal of gaseous HCBz on Cu doped OMS: Effect of Cu location on catalytic performance. *Appl. Catal., B* **2014**, 150–151, 167–178.

(41) Gallastegi-Villa, M.; Aranzabal, A.; Romero-Sáez, M.; González-Marcos, J. A.; González-Velasco, J. R. Catalytic activity of regenerated catalyst after the oxidation of 1,2-dichloroethane and trichloroethylene. *Chem. Eng. J.* **2014**, 241, 200–206.

(42) Aranzabal, A.; Romero-Sáez, M.; Elizundia, U.; González-Velasco, J. R.; González-Marcos, J. A. Deactivation of H-zeolites during catalytic oxidation of trichloroethylene. *J. Catal.* **2012**, 296, 165–174.

(43) Hisham, M. W. M.; Benson, S. W. Thermochemistry of the Deacon process. *J. Phys. Chem.* **1995**, 99 (16), 6194–6198.

(44) Over, H.; Schomäcker, R. What makes a good catalyst for the deacon process? *ACS Catal.* **2013**, 3 (5), 1034–1046.

(45) Amrute, A. P.; Mondelli, C.; Moser, M.; Novell-Leruth, G.; López, N.; Rosenthal, D.; Farra, R.; Schuster, M. E.; Teschner, D.; Schmidt, T. Performance, structure, and mechanism of CeO_2 in HCl oxidation to Cl_2 . *J. Catal.* **2012**, 286, 287–297.

(46) Amrute, A. P.; Mondelli, C.; Hevia, M. A. G.; Perez-Ramirez, J. Mechanism-performance relationships of metal oxides in catalyzed HCl oxidation. *ACS Catal.* **2011**, 1 (6), 583–590.

(47) Lee, J. E.; Jurng, J. Catalytic conversions of polychlorinated benzenes and dioxins with low-chlorine using $\text{V}_2\text{O}_5/\text{TiO}_2$. *Catal. Lett.* **2008**, 120 (3–4), 294–298.